Supporting Information for "Promising regions for detecting the overturning circulation in Atlantic Pa/Th: a model-data comparison"

Jeemijn Scheen[1,2,3], Jörg Lippold[4], Frerk Pöppelmeier[1,2], Finn Süfke[4],

Thomas F. Stocker[1,2]

[1]Climate and Environmental Physics, Physics Institute, University of Bern, Bern, Switzerland

[2]Oeschger Centre for Climate Change Research, University of Bern, Bern, Switzerland

[3]Department of Estuarine and Delta Systems, NIOZ Royal Netherlands Institute for Sea Research, Yerseke, The Netherlands

[4]Institute of Earth Sciences, Heidelberg University, Heidelberg, Germany

Contents of this file

1. Text S1: Data processing of nepheloid-layer maps
2. Text S2: Tuning the Pa and Th module
3. Text S3: Computing the Pa and Th budget
4. References for this file
5. Tables S1 to S2
6. Figures S1 to S7

Additional Supporting Information

1. Caption for Dataset S1: Sediment measurements
2. Caption for Dataset S2: Age models used for this study
3. Caption for Dataset S3: Literature compilation of scavenging parameters

---

Corresponding author: J. Scheen (jeemijn.scheen@nioz.nl)

February 6, 2024, 1:32am

1. Text S1: Data processing of nepheloid-layer maps

Nepheloid-layer height and vertically integrated excess particulate matter mass were used from Gardner, Richardson, Mishonov, and Biscaye (2018a), as described in the main text. These variables were regridded to the Bern3D grid, choosing a bi-linear interpolation method, which uses the 4 neighbouring cells such that the nepheloid-layer information stays local (Fig. S1a,b). As the model needs a value for every cell, we filled data gaps with an algorithm that averages direct neighbours. First all data-gap cells of which all 4 neighbours have a value, i.e., single-cell data gaps, are filled with the average of their neighbours. Then, this is repeated for all data-gaps cells with 3 neighbours with values, etc. Fig. S1c shows the result.

2. Text S2: Tuning the Pa and Th module

Multiple attempts were made to establish a robust way of tuning, finally choosing an approach consisting of three steps that optimise 1) w_s, 2) k^j_{des} and 3) σ^j_i (Sect. 2.5 of the main text). Here we give more details on the final tuning procedure and we share lessons learned from earlier attempts.

Boundaries of the parameter space

Literature studies with observational estimates of K^j_i are compiled and converted to σ^j_i in the Supplement. The resulting range of observations in Table 3 of the main text spans multiple orders of magnitude for most σ^j_i. This makes the parameter space to explore very large, especially when considering that the σ^j_i values that give the best fit for our model could even lie outside of this range due to model errors or inaccurate parameter values for w_s and k^j_{des}. To deal with this, we ran a large number of simulations and cautiously interpreted the results. Since test runs at the maximum observational σ^j_i's still gave good results in the Bern3D model, we ran all tuning ensembles up to twice the observational maximum. Thus, we tuned σ^j_i between the observational minimum and twice the observational maximum.

Tuning boundaries for w_s were set from 500 to 5000 m/yr, where the original model value was $w_s = 1000$ m/yr. This entire range lies at the very low end of observed particle sinking speeds; most observations are at least 5000 m/yr, both for small and large particles (Cael et al., 2021). However, the Bern3D model cannot simulate above 10 km/yr as the CFL criterion would be violated due to its long time step. Boundaries for k^j_{des} are chosen from 1 to 5/yr (with an original model value of 2.4/yr) based on Fig. S2 (see main

text). This is slightly broader than the 1 to 3/yr as given in Luo and Ku (2004a) for Th. Sampling of the parameter space was done via Latin hypercube sampling, assuming a uniform distribution for each parameter.

Determining the final σ_i^j

Section 2.5 of the main text outlines the results of tuning step one and two (w_s = 1600 m/yr and k_{des}^j = 4.0/yr). The third tuning step is to determine σ_i^j. Figure S3 shows the runs of that ensemble sorted by score for MAE_{Pad}, MAE_{Thd}, MAE_{Pap} and MAE_{Thp}. Pa and Th are simulated completely independent in this ensemble, because the only parameter that concerns both, w_s, is fixed. The MAE score of the dissolved forms is more sensitive to parameter changes than the particle-bound form; especially for $\mathrm{Th_p}$, the MAE barely reacts. For Pa as well as for Th, the 10 best runs for the dissolved form are not necessarily good runs for the particle-bound form and vice versa. As the best result for Pa parameters, we choose the σ_i^j of the run that belongs to the best 10 $\mathrm{Pa_d}$ runs and has the best $\mathrm{Pa_p}$ score of those 10; analogously for Th. This corresponds to the first orange (blue) circle in the MAE_{Pap} (MAE_{Thp}) panel of Fig. S3. For Pa, this indicated best run is at position 7 of MAE_{Pad} and at position 148 of MAE_{Pap}; for Th, the best run is also at position 7 of MAE_{Thd} and at position 486 of MAE_{Thp}. The scavenging coefficients σ_i^j of the corresponding run for Pa respectively Th are given in Table 3 of the main text as the σ_i^j tuning result.

Lessons learned from previous attempts

Our first tuning attempt (not mentioned in the main text) was running a large ensemble that varied all parameters (w_s, k_{des}^j, σ_i^j) simultaneously. The first ensemble we ran in this

way varied all σ_i^j until very high values, approximately following the boundaries of the modelling study by Missiaen et al. (2020a). In the Bern3D model, these high σ_i^j gave poor results; optimal runs had σ_i^j within or closer to the observational range. We could not confirm the necessity of the high tuning boundaries of Missiaen et al. (2020a) and their resulting (very high) best σ_i^j values (Table 3 of the main text). We suspect there could be a mistake in the conversion from K_i^j to σ_i^j in their Supplement.

In ensemble 2, we repeated the same approach but now constrained σ_i^j to the observational range. In both ensemble 1 and 2, the results contained no clear parameter minima but rather a lot of scatter when plotting each parameter against the MAE of model-data misfit. Although by definition always 1 run has the minimal MAE, other runs with very similar small MAE had completely different parameter sets. Hence, the best fit cannot be uncritically trusted. Model-data misfit was not caused by outliers, but a certain misfit occurred in all basins and depths. Nevertheless, ensemble 2 was useful to determine w_s since clear minima were present for MAE_{Pap} and MAE_{Thp} with respect to the sinking speed (see main text and Fig. 4 of the main text).

Varying only 1 parameter at a time was investigated in a third ensemble. So instead of sampling random points in the 13-dimensional parameter space, we now moved from a certain fixed starting point along the 13 axes, in 13 sub-ensembles. This resulted in very clear MAE minima, for example shaped as parabola. However, combining the optimal values found for each parameter in 1 simulation, resulted in surprisingly bad MAEs. Apparently, the parameter space is very sensitive to the starting point; the landscape has a lot of hills and slopes. Concluding, varying all (w_s, k_{des}^j, σ_i^j) simultaneously did not

work nor did varying all 13 independently. So after fixing w_s, we fixed k^j_{des} and then all σ^j_i in additional ensembles (main text).

The reason for MAE scatter is that parameters are not truly independent in the model. Sinking speed governs the total inventory and can cause a global model-data offset, dominating MAE changes by other parameters. Therefore w_s is tuned and fixed first. Intuitively, increasing the desorption constant k^{Pa}_{des} is similar to decreasing all σ^{Pa}_i with the same factor. Therefore two parameter sets can create identical results, causing scatter. Variations within the σ^j_i also generate a part of the scatter such that scatter is still present in our final tuning approach (projections in Fig. S4). While varying all σ^j_i, we vary their mutual ratios as well as the 'total scavenging', which can be quantified as, e.g., $\sum_i \sigma^j_i$. For instance, if the total scavenging is very high, then the all-abundant particles take so much Pa and Th out of the water column that all modelled values are lower than observed. This will yield a bad MAE, even if the mutual ratios of σ^j_i are very good.

3. Text S3: Computing the Pa and Th budget

Deng, Henderson, Castrillejo, Perez, and Steinfeldt (2018) computed the present-day budget and meridional fluxes of Pa and Th in the Atlantic based on seawater measurements. We repeat their approach, now based on the Bern3D model CTRL run. The result is shown in Fig. 7b of the main text, with boundaries and transects in Fig. C2 of the main text. In this section, we share the details of the computation. The used python scripts are also published along, together with the code to generate all figures.

Table S1 lists the Pa and Th fluxes through each transect. All contributions to the budget are combined in Table S2. The total production slightly differs from Deng et al. (2018) as the water volume in the Bern3D model depends on the bathymetry of the grid cells. In our case we are also able to compute the fraction that is removed to the sediment within the sub-basin, by multiplying the $\mathrm{Pa_p}$ or $\mathrm{Th_p}$ concentration in the bottommost grid cells with sinking speed w_s, grid cell area and density. The contributions of meridional transport by advection and removal to the sediment do not exactly add up to the total production: the residual we find (Table S2) represents diffusion due to horizontal gradients in Pa and Th plus uncertainties in the model. The residual is only 2 to 5 % of the production in all cases except for Pa in the South Atlantic. Here, the residual indicates a 16 % diffusive flux of Pa out of the South Atlantic. This possibly originates from the southern opal belt: high opal concentrations in the Southern Ocean induces a diffusive flux of $\mathrm{Pa_d}$ directed out of the South Atlantic into the Southern Ocean.

References

Blaauw, M., & Christen, J. A. (2011). Flexible paleoclimate age-depth models using an autoregressive gamma process. *Bayesian Analysis*, *6*, 457–474. doi: 10.1214/11-BA618

Cael, B. B., Cavan, E. L., & Britten, G. L. (2021). Reconciling the size-dependence of marine particle sinking speed. *Geophysical Research Letters*, *48*, e2020GL091771. doi: 10.1029/2020GL091771

Chase, Z., & Anderson, R. F. (2004). Comment on "on the importance of opal, carbonate, and lithogenic clays in scavenging and fractionating 230Th, 231Pa and 10Be in the ocean"' by S. Luo and T.-L. Ku. *Earth and Planetary Science Letters*, *220*, 213–222. doi: 10.1016/S0012-821X(04)00028-7

Chase, Z., Anderson, R. F., Fleisher, M. Q., & Kubik, P. W. (2002). The influence of particle composition and particle flux on scavenging of Th, Pa and Be in the ocean. *Earth and Planetary Science Letters*, *204*, 215–229. doi: 10.1016/S0012-821X(02)00984-6

Deng, F., Henderson, G. M., Castrillejo, M., Perez, F. F., & Steinfeldt, R. (2018). Evolution of ^{231}Pa and ^{230}Th in overflow waters of the North Atlantic. *Biogeosciences*, *15*, 7299–7313. doi: 10.5194/bg-15-7299-2018

Gardner, W. D., Richardson, M. J., Mishonov, A. V., & Biscaye, P. E. (2018a). Global comparison of benthic nepheloid layers based on 52 years of nephelometer and transmissometer measurements. *Progress in Oceanography*, *168*, 100–111. doi: 10.1016/j.pocean.2018.09.008

Geibert, W., & Usbeck, R. (2004). Adsorption of thorium and protactinium onto different particle types: experimental findings. *Geochimica et Cosmochimica Acta*, *68*, 1489–1501. doi: 10.1016/j.gca.2003.10.011

Gottschalk, J., Szidat, S., Michel, E., Mazaud, A., Salazar, G., Battaglia, M., Lippold, J., & Jaccard, S. L. (2018). Radiocarbon measurements of small-size foraminiferal samples with the Mini Carbon Dating System (MICADAS) at the University of Bern: Implications for paleoclimate reconstructions. *Radiocarbon*, *60*, 469—491. doi: 10.1017/RDC.2018.3

Hayes, C. T., Anderson, R. F., Fleisher, M. Q., Vivancos, S. M., Lam, P. J., Ohnemus, D. C., Huang, K.-F., Robinson, L. F., Lu, Y., Cheng, H., Edwards, R. L., & Moran, S. B. (2015a). Intensity of Th and Pa scavenging partitioned by particle chemistry in the North Atlantic Ocean. *Marine Chemistry*, *170*, 49–60. doi: 10.1016/j.marchem.2015.01.006

Heaton, T. J., Köhler, P., Butzin, M., Bard, E., Reimer, R. W., Austin, W. E. N., Bronk Ramsey, C., Grootes, P. M., Hughen, K. A., Kromer, B., Reimer, P. J., Adkins, J., Burke, A., Cook, M. S., Olsen, J., & Skinner, L. C. (2020). Marine20 — the marine radiocarbon age calibration curve (0–55,000 cal BP). *Radiocarbon*, *62*, 779—820. doi: 10.1017/RDC.2020.68

Jones, G. A., Johnson, D. A., & Curry, W. B. (1984). High-resolution stratigraphy in late Pleistocene/Holocene sediments of the Vema Channel. *Marine Geology*, *58*, 59–87. doi: 10.1016/0025-3227(84)90116-6

Lippold, J., Gutjahr, M., Blaser, P., Christner, E., de Carvalho Ferreira, M. L., Mulitza,

S., Christl, M., Wombacher, F., Böhm, E., Antz, B., Cartapanis, O., Vogel, H., & Jaccard, S. L. (2016). Deep water provenance and dynamics of the (de)glacial Atlantic meridional overturning circulation. *Earth and Planetary Science Letters*, *445*, 68–78. doi: 10.1016/j.epsl.2016.04.013

Luo, S., & Ku, T.-L. (2004a). On the importance of opal, carbonate, and lithogenic clays in scavenging and fractionating 230Th, 231Pa and 10Be in the ocean. *Earth and Planetary Science Letters*, *220*, 201–211. doi: 10.1016/S0012-821X(04)00027-5

Luo, S., & Ku, T.-L. (2004b). Reply to Comment on "On the importance of opal, carbonate, and lithogenic clays in scavenging and fractionating 230Th, 231Pa and 10Be in the ocean". *Earth and Planetary Science Letters*, *220*, 223–229. doi: 10.1016/S0012-821X(04)00029-9

Mahowald, N. M., Albani, S., Kok, J. F., Engelstaeder, S., Scanza, R., Ward, D. S., & Flanner, M. G. (2014). The size distribution of desert dust aerosols and its impact on the Earth system. *Aeolian Research*, *15*, 53–71. doi: 10.1016/j.aeolia.2013.09.002

Max, L., Nürnberg, D., Chiessi, C. M., Lenz, M. M., & Mulitza, S. (2022). Subsurface ocean warming preceded Heinrich Events. *Nature Communications*, *13*, 4217. doi: 10.1038/s41467-022-31754-x

Missiaen, L., Bouttes, N., Roche, D. M., Dutay, J.-C., Quiquet, A., Waelbroeck, C., Pichat, S., & Peterschmitt, J.-Y. (2020a). Carbon isotopes and Pa/Th response to forced circulation changes: a model perspective. *Climate of the Past*, *16*, 867–883. doi: 10.5194/cp-16-867-2020

Missiaen, L., Waelbroeck, C., Pichat, S., Jaccard, S. L., Eynaud, F., Greenop, R., & Burke, A. (2019). Improving North Atlantic marine core chronologies using 230Th normalization. *Paleoceanography and Paleoclimatology*, *34*, 1057–1073. doi: 10.1029/2018PA003444

Roy-Barman, M., Foliot, L., Douville, E., Leblond, N., Gazeau, F., Bressac, M., Wagener, T., Ridame, C., Desboeufs, K., & Guieu, C. (2021). Contrasted release of insoluble elements (Fe, Al, rare earth elements, Th, Pa) after dust deposition in seawater: a tank experiment approach. *Biogeosciences*, *18*, 2663–2678. doi: 10.5194/bg-18-2663-2021

Tessin, A. C., & Lund, D. C. (2013). Isotopically depleted carbon in the mid-depth South Atlantic during the last deglaciation. *Paleoceanography*, *28*, 296–306. doi: 10.1002/palo.20026

Waelbroeck, C., Lougheed, B. C., Vazquez Riveiros, N., Missiaen, L., Pedro, J., Dokken, T., Hajdas, I., Wacker, L., Abbott, P., Dumoulin, J.-P., Thil, F., Eynaud, F., Rossignol, L., Fersi, W., Albuquerque, A. L., Arz, H., Austin, W. E. N., Came, R., Carlson, A. E., Collins, J. A., Dennielou, B., Desprat, S., Dickson, A., Elliot, M., Farmer, C., Giraudeau, J., Gottschalk, J., Henderiks, J., Hughen, K., Jung, S., Knutz, P., Lebreiro, S., Lund, D. C., Lynch-Stieglitz, J., Malaizé, B., Marchitto, T., Martínez-Méndez, G., Mollenhauer, G., Naughton, F., Nave, S., Nürnberg, D., Oppo, D., Peck, V., Peeters, F. J. C., Penaud, A., Portilho-Ramos, R. d. C., Repschläger, J., Roberts, J., Rühlemann, C., Salgueiro, E., Sanchez Goni, M. F., Schönfeld, J., Scussolini, P., Skinner, L. C., Skonieczny, C., Thornalley, D., Toucanne, S., Rooij, D. V., Vidal, L., Voelker, A. H. L., Wary, M., Weldeab, S., & Ziegler, M. (2019). Consistently dated

Atlantic sediment cores over the last 40 thousand years. *Scientific Data*, *6*, 165. doi: 10.1038/s41597-019-0173-8

Zhang, X., Yang, W., Qiu, Y., & Zheng, M. (2021). Adsorption of Th and Pa onto particles and the effect of organic compounds in natural seawater. *Journal of Oceanology and Limnology*, *39*, 2209–2219. doi: 10.1007/s00343-021-0297-5

Table S1. Transport of Pa_d and Th_d by water advection across three Atlantic transects and into the Mediterranean (Fig. C2 of the main text) for the CTRL run.

	Pa_d transport across section $\times 10^{10}$ μBq/s	Th_d transport across section $\times 10^{10}$ μBq/s
GEOVIDE[a]	-0.279	-3.321
WOCE A07[a]	-4.344	-6.975
WOCE A11[a]	-5.550	-10.868
MED[b]	0.0135	0.0175

[a]Positive values indicate northward transport; negative values indicate southward transport.
[b]Positive values indicate eastward transport from the Atlantic to the Mediterranean Sea.

Table S2. Water volume and budget of Pa and Th in the North Atlantic (NAtl) and South Atlantic (SAtl) sub-basins (Fig. C2 of the main text), based on the CTRL run. Source terms for the sub-basin are shown as positive values; sinks negative.

	Water volume	Production	Adv. merid. transport[a,b]	Removal to sediment	Residual[a,c]	Adv. merid. transport / production
	$\times 10^{17}$ m^3	$\times 10^{10}$ μBq/s	$\times 10^{10}$ μBq/s	$\times 10^{10}$ μBq/s	$\times 10^{10}$ μBq/s	%
Pa in NAtl	1.521	18.72	-4.08[d]	-14.26	-0.38	21.8 %
Pa in SAtl	0.9876	12.15	-1.21[e]	-8.96	-1.98	10.0 %
Th in NAtl	1.521	202.5	-3.67[d]	-190.9	-7.93	1.8 %
Th in SAtl	0.9876	131.4	-3.89[e]	-121.1	-6.41	3.0 %

[a]Positive values mean net transport is directed into the sub-basin; negative if out of the sub-basin.
[b]Net meridional transport by advection.
[c]Represents horizontal diffusion of Pa or Th plus model uncertainty.
[d]For NAtl: WOCE_A07 - GEOVIDE - MED (Table S1).
[e]For SAtl: WOCE_A11 - WOCE_A07 (Table S1).

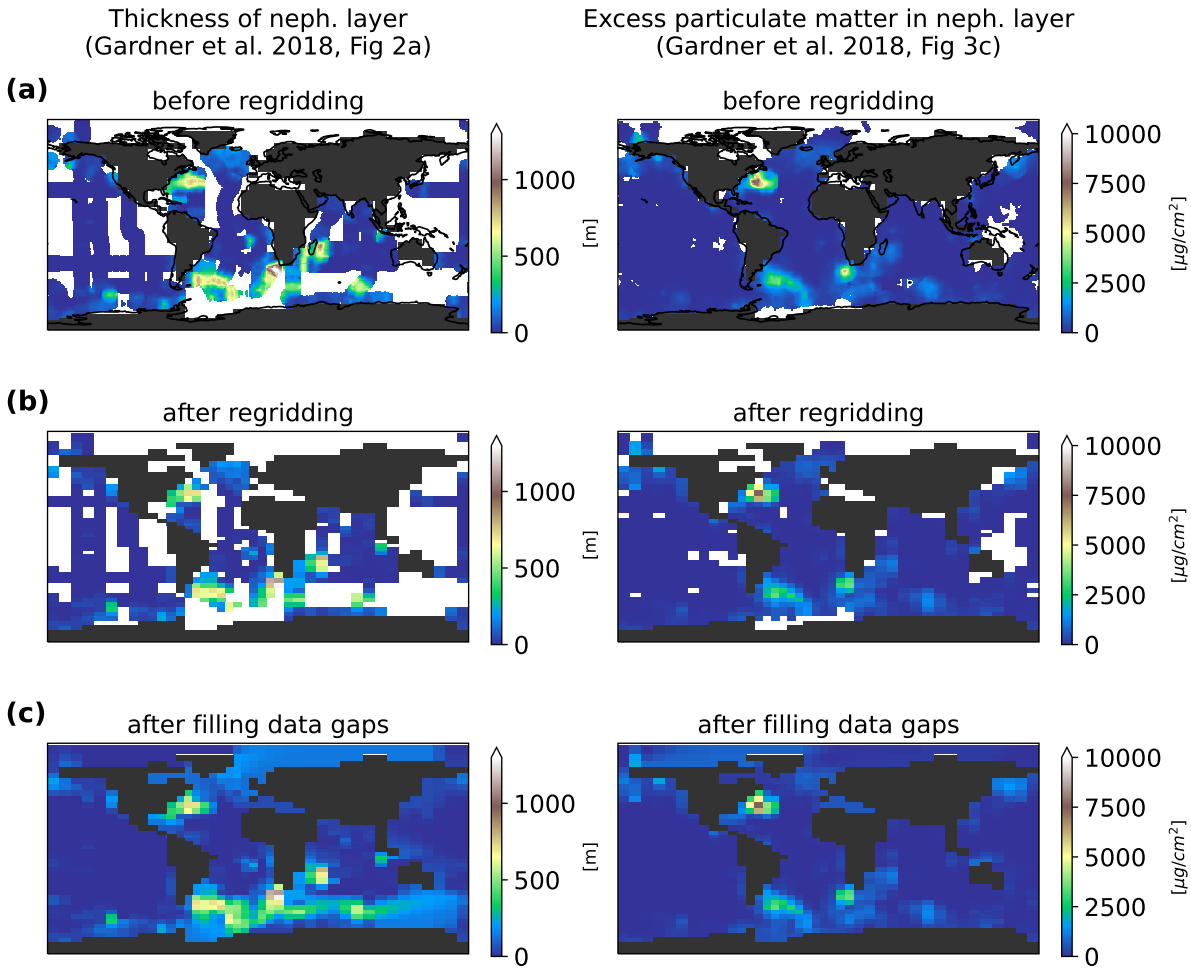

Figure S1. **(a)** Nepheloid-layer thickness (left) and excess concentration of nepheloid particulate matter, integrated over the nepheloid-layer thickness, (right) from Gardner et al. (2018a), their figures 2a and 3c, respectively. Data are plotted on a 1°×1° grid and white ocean surfaces represent data gaps. **(b)** After regridding to the Bern3D grid. **(c)** After regridding and filling the data gaps.

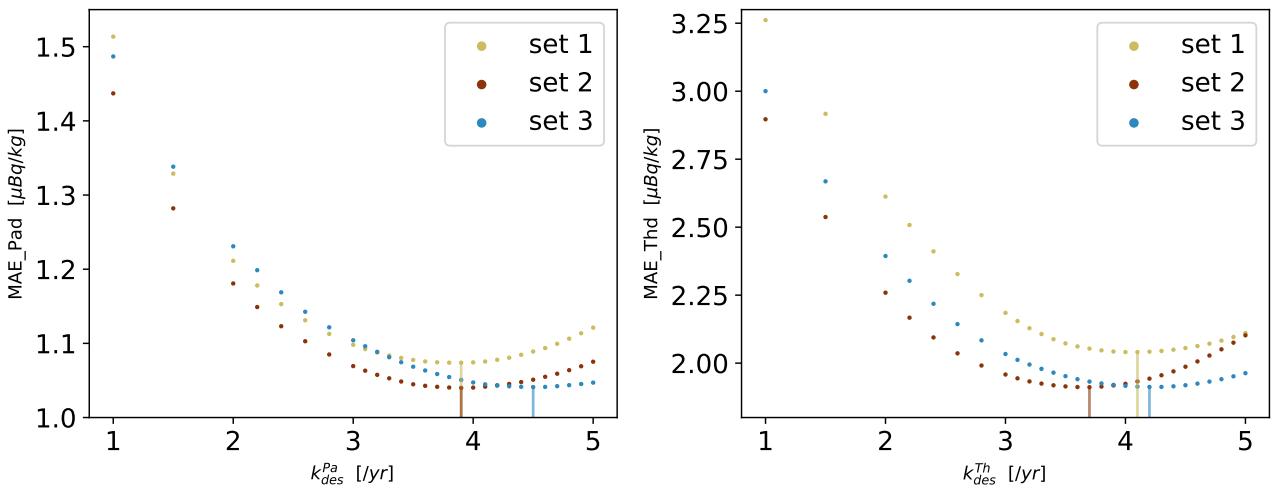

Figure S2. Mean Absolute Error (MAE) score for variables Pa_d and Th_d for 3×28 simulations that vary the desorption coefficient k_{des}^{j}, while holding the other parameters constant (see 3 parameter sets in Table 3 of the main text). Desorption coefficients that minimise the MAE are indicated by vertical lines in the corresponding colour: 3.9, 3.9 and 4.5/yr resp. for k_{des}^{Pa}; and 4.1, 3.7 and 4.2/yr resp. for k_{des}^{Th}.

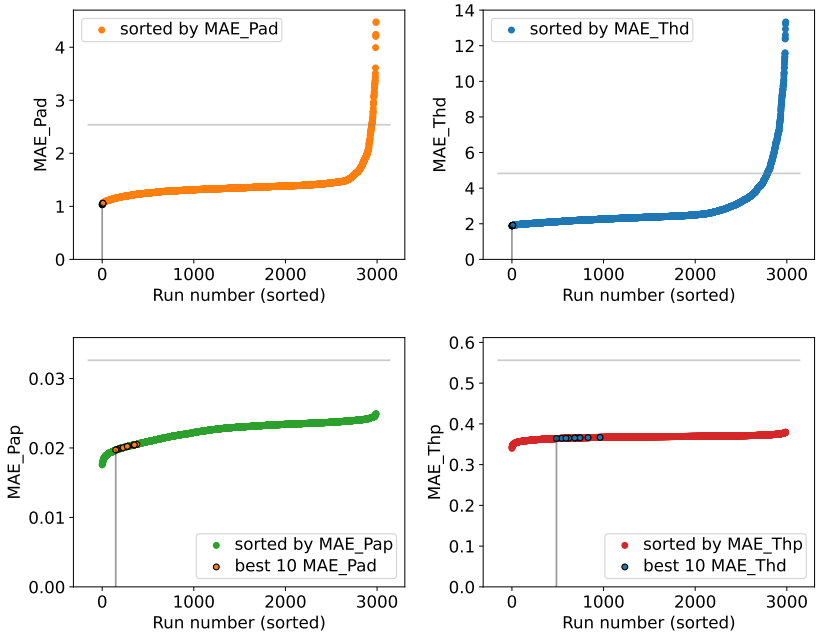

Figure S3. 3000 simulations varying σ_i^j under constant $w_s = 1600$ m/yr and $k_{des}^j = 4.0$/yr, sorted by their Mean Absolute Error (MAE) score for variables $\mathrm{Pa_d}$, $\mathrm{Th_d}$, $\mathrm{Pa_p}$ and $\mathrm{Th_p}$. The 10 simulations with the best scores for $\mathrm{Pa_d}$ (i.e., runs 0-9 in the $\mathrm{Pa_d}$ plot) are indicated in orange in the subplot for $\mathrm{Pa_p}$, and analogously for Th. Conclusion of best runs for Pa and for Th are indicated by vertical lines with corresponding σ_i^j in Table 3 of the main text. Horizontal grey lines indicate MAEs for a hypothetical model simulation with output 0 in every grid cell: MAEs around and above these lines are very poor. The 10 runs with highest MAE are omitted for better visibility.

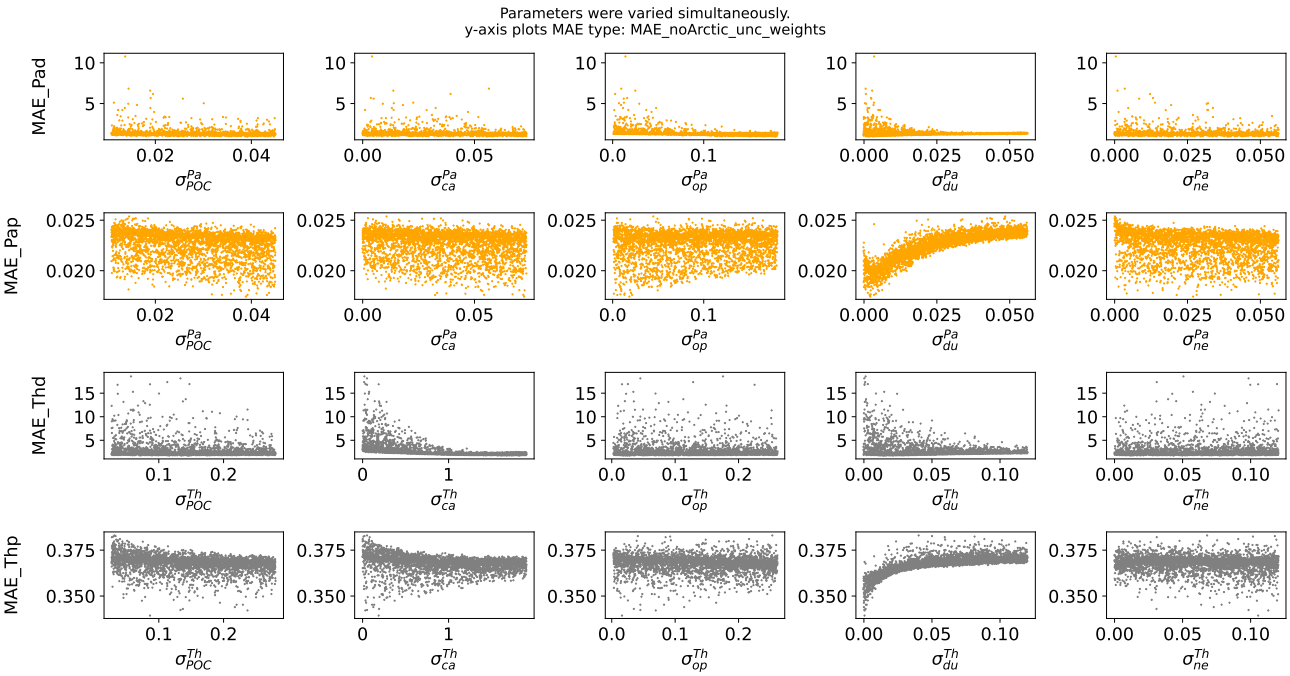

Figure S4. Mean Absolute Error (MAE) scores for variables Pa_d, Th_d, Pa_p and Th_p per scavenging coefficient σ_i^j over the 3000-member ensemble that varies all σ_i^j simultaneously (fixing $w_s = 1600$ m/yr and $k_{des}^j = 4.0$/yr).

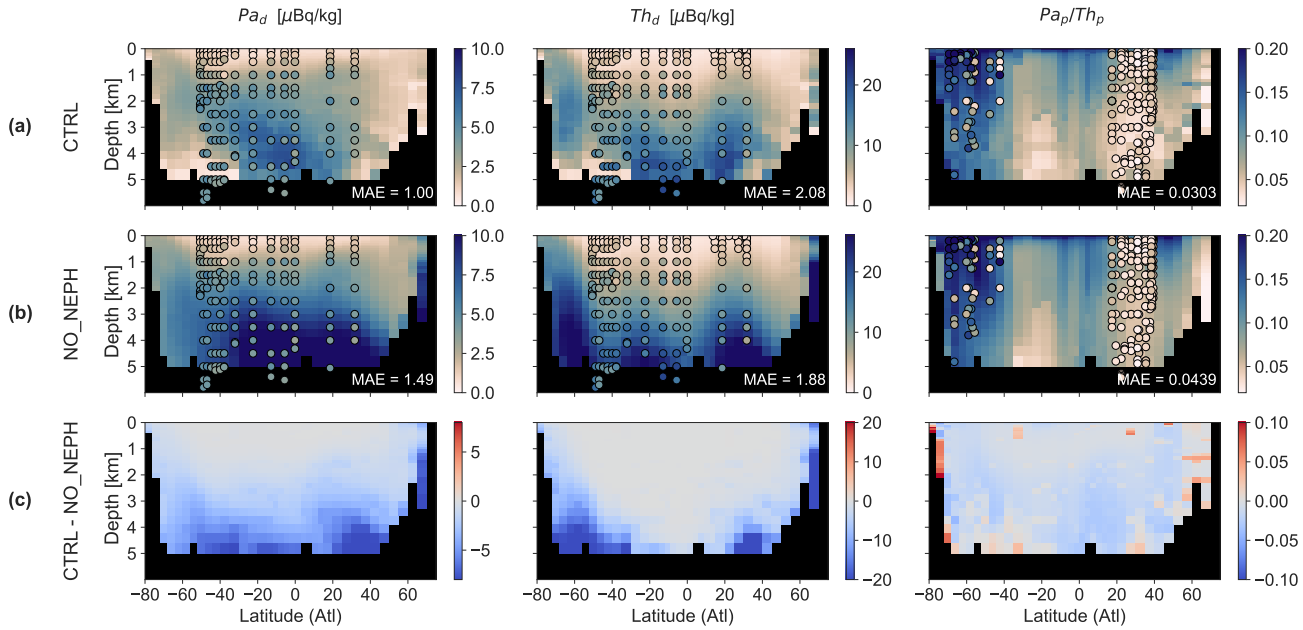

Figure S5. Atlantic dissolved Pa_d, Th_d and the particle-bound ratio Pa_p/Th_p for pre-industrial conditions. Circles show Pa_d and Th_d seawater observations in the West Atlantic (GA02), respectively Pa_p/Th_p seawater observations in the entire Atlantic (GA03 and GIPY05); references in section 2.3 of the main text. Background colours show Atlantic zonal average model output for **(a)** the CTRL simulation; **(b)** the NO_NEPH simulation, and **(c)** their anomaly. Mean absolute errors (MAEs) are indicated. MAEs were taken between the observations shown in the respective panel and the model run shown in the respective panel, where the model grid cell closest to each observation was used (i.e., not using the plotted zonal average). MAEs were computed in the usual way (weighted by observational uncertainty and averaging if multiple observations lie within one grid cell; see main text).

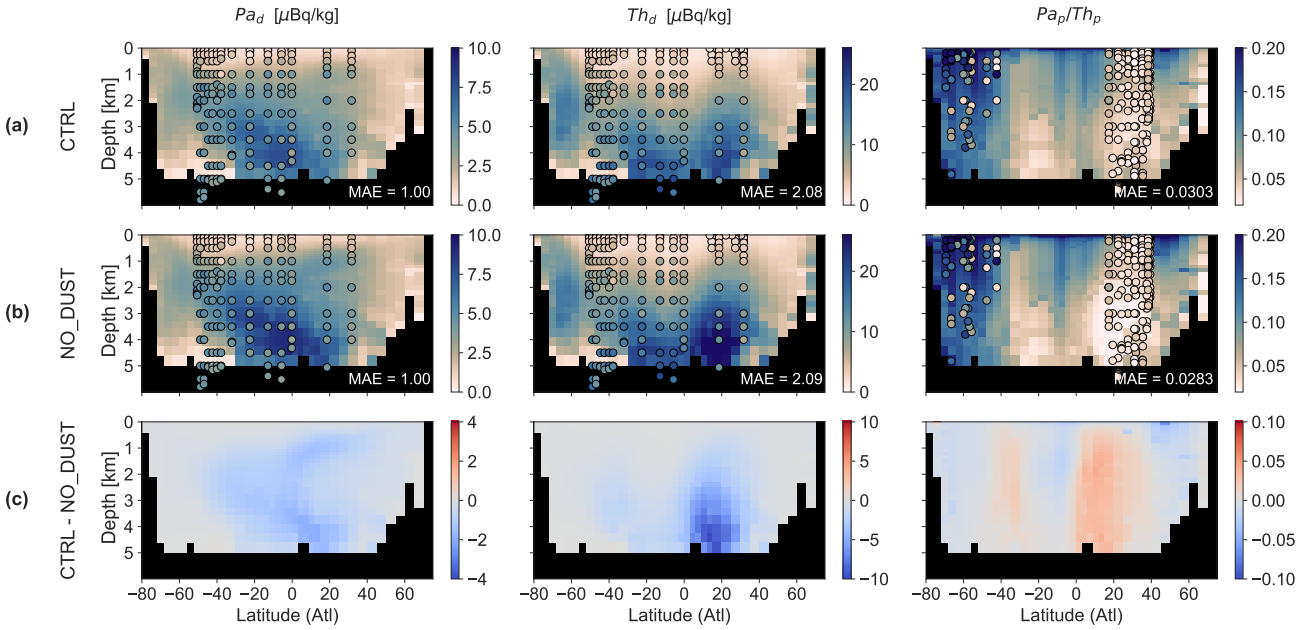

Figure S6. As in Fig. S5 but for a simulation without dust. Background colours show Atlantic zonal average model output for **(a)** the CTRL simulation; **(b)** the NO_DUST simulation, and **(c)** their anomaly. Note that the anomaly colour scales in panels c differ between Fig. S5-S7.

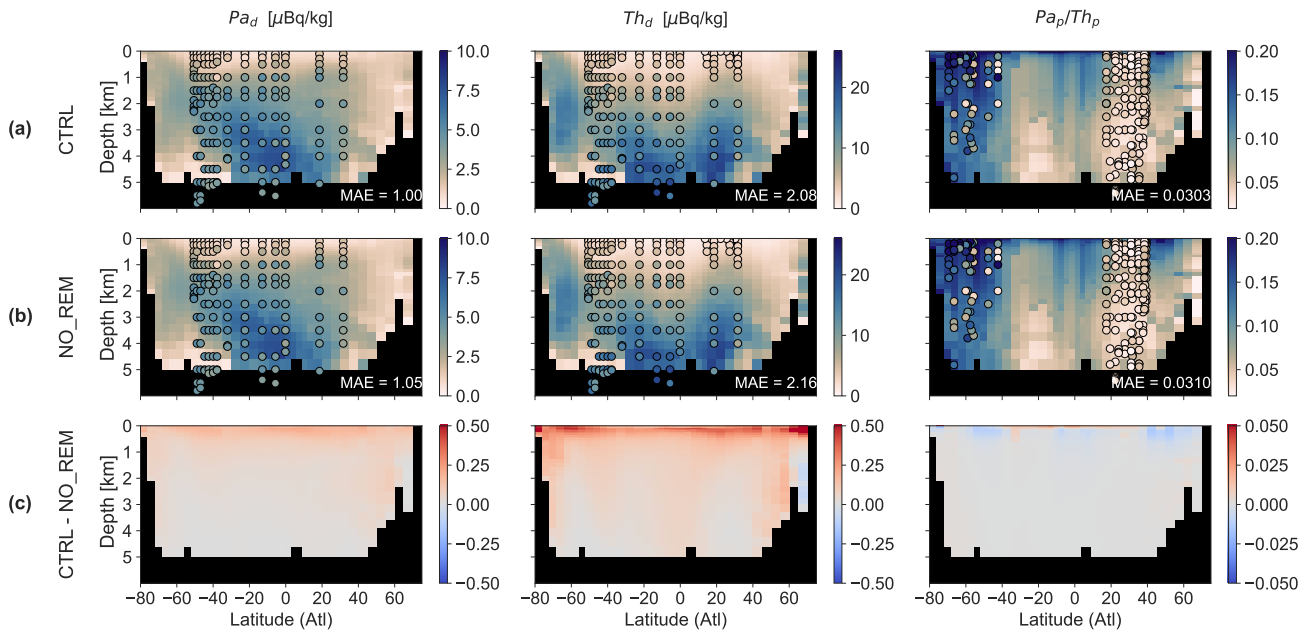

Figure S7. As in Fig. S5 but for a simulation without dust. Background colours show Atlantic zonal average model output for **(a)** the CTRL simulation; **(b)** the NO_REM simulation, which has the remineralisation term disabled, and **(c)** their anomaly. Note that the anomaly colour scales in panels c differ between Fig. S5-S7.

Dataset S1. Sediment measurements: Dataset 1_sediment_measurements.xlsx contains the contents of Table 2 from the main text. This file is directly read in in the analysis code for the figures. The index # refers to the map in Fig. 3a of the main text; 'Pa/Th' is the average of 'n' samples in the time interval; SE is the standard error; and region numbers refer to Fig. 3b of the main text. Dataset S2 contains the individual samples of the newly published cores.

Dataset S2. Age models used for this study: Dataset 2_age_models.xlsx contains the raw data of the newly published cores as well as the age models of these cores. Note the two tabs in the excel file. The indicated references used for the different age models are: Blaauw and Christen (2011); Gottschalk et al. (2018); Heaton et al. (2020); Jones, Johnson, and Curry (1984); Lippold et al. (2016); Max, Nürnberg, Chiessi, Lenz, and Mulitza (2022); Missiaen et al. (2019); Tessin and Lund (2013); Waelbroeck et al. (2019).

Dataset S3. Literature compilation of scavenging parameters: the first tab of Dataset 3_compilation_Kd_to_sigma.xlsx contains a compilation of partition coefficients $(K_d)_i^j = K_i^j$ from the observational studies: Chase, Anderson, Fleisher, and Kubik (2002); Geibert and Usbeck (2004); Hayes et al. (2015a); Luo and Ku (2004a) and Zhang, Yang, Qiu, and Zheng (2021). Other references used here are Mahowald et al. (2014); Roy-Barman et al. (2021) and the discussion in Chase and Anderson (2004) and Luo and Ku (2004b). The resulting literature range of partition coefficients $(K_d)_i^j$ from tab 1 is converted on tab 2 to a range of scavenging coefficients σ_i^j using (Missiaen et al., 2020a). The resulting σ_i^j range is shown as 'Min obs.' and 'Max obs' in Table 3 of the main text.